REPORT DOCUMENTATION PAGE

Form Approved
OMB No. 0704-0188

1. REPORT DATE *(DD-MM-YYYY)*	**2. REPORT TYPE**	**3. DATES COVERED** *(From – To)*
14 une 2018	Journal Article	01-02-2014 to 01-02-2016

4. TITLE AND SUBTITLE

Probe beam deflection optical imaging of thermal and electrostrictive phenomena resulting from nano-second electric pulse exposure (nsEP) in vitro

5a. CONTRACT NUMBER
In-house

5b. GRANT NUMBER

5c. PROGRAM ELEMENT NUMBER
62202F

6. AUTHOR(S)

Ronald A Barnes1,2, Caleb C Roth2,4 , Hope T. Beier3 , Gary Noojan3, Christopher M. Valdez1,2, Joel N. Bixler3, Mehdi Shadaram5 and Bennett L. Ibey2

5d. PROJECT NUMBER
7757

5e. TASK NUMBER
B3

5f. WORK UNIT NUMBER
60/H0AW

7. PERFORMING ORGANIZATION NAME(S) AND ADDRESS(ES)

1National Research Council, Oak Ridge Institute for Science and Education, JBSA Fort Sam Houston, TX, 78234
2 Radio Frequency Bioeffects Branch, Bioeffects Division, Airman Systems Directorate, Air Force Research Laboratory, , JBSA Fort Sam Houston, Texas, 78234
3 Optical Radiation Bioeffects Branch, Bioeffects Division, Airman Systems Directorate, Air Force Research Laboratory, JBSA Fort Sam Houston, Texas, 78234
4School of Medicine, Dept. of Radiological Sciences, University of Texas Health Science Center San Antonio, 7703 Floyd Curl Drive, San Antonio, TX, 78229
5Electrical Engineering Department, The University of Texas at San Antonio, San Antonio, Texas 78249

8. PERFORMING ORGANIZATION REPORT NUMBER

N/A

9. SPONSORING / MONITORING AGENCY NAME(S) AND ADDRESS(ES)

Air Force Material Command, Air Force Research Laboratory, 711th Human Performance Wing, Human Effectiveness Directorate, Bioeffects Division, XXXXX Branch (711 HPW/RHDX)

10. SPONSOR/MONITOR'S ACRONYM(S)
711 HPW/RHD_

11. SPONSOR/MONITOR'S REPORT NUMBER(S)
AFRL-RH-FS-JA-2017-0005

12. DISTRIBUTION / AVAILABILITY STATEMENT

Distribution A. Approved for public release, distribution unlimited; PA # TSRL 17-0127, 20 Jan 2017.

13. SUPPLEMENTARY NOTES

14. ABSTRACT

The biological effects of nanosecond-duration electric pulses (nsEP) have been studied extensively and are theorized to induce temporary nanoporation of plasma membranes of eukaryotic cells in vitro and in vivo. The physical to biological driving mechanisms behind nanoporation still remain unclear, but could be a result of a multitude of stimuli, including mechanical (shockwaves, electrodeformation), thermal, and electrical (ion transport, channel gating). Experimentally quantifying and characterizing mechanical fields with piezoelectric transducers proves difficult due to electromagnetic interference (EMI) generated by nsEP pulses. The probe beam deflection technique is a passive optical method for quantifying refractive index gradients in liquids and gases that probes both dynamic and static events. In this work, a probe beam deflection imaging system was designed to acquire 2-D images of thermal/mechanical near and far field phenomena resulting from monopolar and bipolar nsEP pulses.

15. SUBJECT TERMS

16. SECURITY CLASSIFICATION OF:			**17. LIMITATION OF ABSTRACT**	**18. NUMBER OF PAGES**	**19a. NAME OF RESPONSIBLE PERSON**
a. REPORT	**b. ABSTRACT**	**c. THIS PAGE**			R. Barnes
Unclassified	Unclassified	Unclassified	SAR	19	**19b. TELEPHONE NUMBER** (include area code) N/A

Standard Form 298 (Rev. 8-98)
Prescribed by ANSI Std. Z39.18

Research Article | Vol. 25, No. 6 | 20 Mar 2017 | OPTICS EXPRESS 6621

Optics EXPRESS

Probe beam deflection optical imaging of thermal and mechanical phenomena resulting from nanosecond electric pulse (nsEP) exposure *in-vitro*

Ronald A Barnes,[1,*] Caleb C Roth,[1] Hope T. Beier,[2] Gary Noojin,[2] Christopher Valdez,[3] Joel Bixler,[2] Erick Moen,[4] Mehdi Shadaram,[5] and Bennett L. Ibey[1]

[1]*Radio Frequency Bioeffects Branch, Bioeffects Division, Airman Systems Directorate, Air Force Research Laboratory,, JBSA Fort Sam Houston, TX 78234,USA*
[2]*Optical Radiation Bioeffects Branch, Bioeffects Division, Airman Systems Directorate, Air Force Research Laboratory, JBSA Fort Sam Houston, TX 78234, USA*
[3]*National Research Council Postdoctoral Fellow, Bioeffects Division, Airman Systems Directorate, Air Force Research Laboratory, JBSA Fort Sam Houston, TX 78234,USA*
[4]*Ming Hsieh Department of Electrical Engineering - Electrophysics, University of Southern California, 920 Bloom Walk, SSC, 502 Los Angeles, CA, USA*
[5]*Electrical Engineering Department, The University of Texas at San Antonio, 1 UTSA Circle, San Antonio, TX 78249, USA*
**ronald.a.barnes.ee@gmail.com*

Abstract: Electric-field induced physical phenomena, such as thermal, mechanical and electrochemical dynamics, may be the driving mechanism behind bioeffects observed in mammalian cells during exposure to nanosecond-duration electric pulses (nsEP) *in-vitro*. Correlating a driving mechanism to a biological response requires the experimental measurement and quantification of all physical dynamics resulting from the nsEP stimulus. A passive and electromagnetic interference (EMI) immune sensor is required to resolve these dynamics in high strength electric fields. The probe beam deflection technique (PBDT) is a passive and EMI immune optical method for quantifying and imaging refractive index gradients in liquids and gases, both dynamic and static, with nanosecond temporal resolution. In this work, a probe beam deflection imaging system was designed to acquire 2-D time-lapse images of thermal/mechanical dynamics resulting from monopolar and bipolar nsEP stimulus.

OCIS codes: (110.0110) Imaging systems; (110.3010) Image reconstruction techniques.

References and links

1. R. Nuccitelli, U. Pliquett, X. Chen, W. Ford, R. James Swanson, S. J. Beebe, J. F. Kolb, and K. H. Schoenbach, "Nanosecond pulsed electric fields cause melanomas to self-destruct," Biochem. Biophys. Res. Commun. **343**(2), 351–360 (2006).
2. P. T. Vernier, Y. Sun, L. Marcu, S. Salemi, C. M. Craft, and M. A. Gundersen, "Calcium bursts induced by nanosecond electric pulses," Biochem. Biophys. Res. Commun. **310**(2), 286–295 (2003).
3. K. H. Schoenbach, B. Hargrave, R. P. Joshi, J. F. Kolb, R. Nuccitelli, C. Osgood, A. Pakhomov, M. Stacey, R. J. Swanson, J. A. White, S. Xiao, J. Zhang, S. Beebe, P. Blackmore, and E. Buescher, "Bioelectric effects of intense nanosecond pulses," IEEE Trans. Dielectr. Electr. Insul. **14**(5), 1088–1109 (2007).
4. K. H. Schoenbach, A. G. Pakhomov, I. Semenov, S. Xiao, O. N. Pakhomova, and B. L. Ibey, "Ion transport into cells exposed to monopolar and bipolar nanosecond pulses," Bioelectrochemistry **103**, 44–51 (2015).
5. A. G. Pakhomov, J. F. Kolb, J. A. White, R. P. Joshi, S. Xiao, and K. H. Schoenbach, "Long-lasting plasma membrane permeabilization in mammalian cells by nanosecond pulsed electric field (nsPEF)," Bioelectromagnetics **28**(8), 655–663 (2007).
6. B. L. Ibey, S. Xiao, K. H. Schoenbach, M. R. Murphy, and A. G. Pakhomov, "Plasma membrane permeabilization by 60- and 600-ns electric pulses is determined by the absorbed dose," Bioelectromagnetics **30**(2), 92–99 (2009).
7. B. L. Ibey, J. C. Ullery, O. N. Pakhomova, C. C. Roth, I. Semenov, H. T. Beier, M. Tarango, S. Xiao, K. H. Schoenbach, and A. G. Pakhomov, "Bipolar nanosecond electric pulses are less efficient at

#279452 https://doi.org/10.1364/OE.25.006621
Journal © 2017 Received 10 Jan 2017; revised 26 Feb 2017; accepted 1 Mar 2017; published 14 Mar 2017

Optics EXPRESS

electropermeabilization and killing cells than monopolar pulses," Biochem. Biophys. Res. Commun. **443**(2), 568–573 (2014).
8. J. Kolb, R. Joshi, S. Xiao, and K. Schoenbach, "Streamers in water and other dielectric liquids," J. Phys. D Appl. Phys. **41**(23), 234007 (2008).
9. D. Kang, J. B. Nah, M. Cho, and S. Xiao, "Shock wave generation in water for biological studies," IEEE Trans. Plasma Sci. **42**(10), 3231–3238 (2014).
10. V. Y. Ushakov, V. F. Klimkin, and S. Korobeynikov, *Impulse Breakdown of Liquids* (Springer Science & Business Media, 2007).
11. J. A. Stratton, *Electromagnetic Theory* (John Wiley & Sons, 2007).
12. L. D. Landau, J. Bell, M. Kearsley, L. Pitaevskii, E. Lifshitz, and J. Sykes, *Electrodynamics of Continuous Media* (Elsevier, 2013), Vol. 8.
13. I. Marinov, O. Guaitella, A. Rousseau, and S. Starikovskaia, "Cavitation in the vicinity of the high-voltage electrode as a key step of nanosecond breakdown in liquids," Plasma Sources Sci. Technol. **22**(4), 042001 (2013).
14. Y. Seepersad, M. Pekker, M. N. Shneider, D. Dobrynin, and A. Fridman, "On the electrostrictive mechanism of nanosecond-pulsed breakdown in liquid phase," J. Phys. D Appl. Phys. **46**(16), 162001 (2013).
15. I. S. Jacobs and A. W. Lawson, "An analysis of the pressure dependence of the dielectric constant of polar liquids," J. Chem. Phys. **20**(7), 1161–1164 (1952).
16. S. Karl, K. Juergen, X. Shu, K. Sunao, M. Yasushi, and J. Ravindra, "Electrical breakdown of water in microgaps," Plasma Sources Sci. Technol. **17**(2), 024010 (2008).
17. L. V. Wang and S. Hu, "Photoacoustic tomography: in vivo imaging from organelles to organs," Science **335**(6075), 1458–1462 (2012).
18. C. C. Roth, R. A. Barnes, Jr., B. L. Ibey, H. T. Beier, L. Christopher Mimun, S. M. Maswadi, M. Shadaram, and R. D. Glickman, "Characterization of pressure transients generated by nanosecond electrical pulse (nsEP) exposure," Sci. Rep. **5**, 15063 (2015).
19. R. A. Barnes, Jr., S. Maswadi, R. Glickman, and M. Shadaram, "Probe beam deflection technique as acoustic emission directionality sensor with photoacoustic emission source," Appl. Opt. **53**(3), 511–519 (2014).
20. J. N. Caron and G. P. DiComo, "Frequency response of optical beam deflection by ultrasound in water," Appl. Opt. **53**(32), 7677–7683 (2014).
21. J. L. Johnson, K. van Wijk, J. N. Caron, and M. Timmerman, "Gas-coupled laser acoustic detection as a non-contact line detector for photoacoustic and ultrasound imaging," J. Opt. **18**(2), 024005 (2016).
22. M. Waxler and C. E. Weir, "Effect of pressure and temperature on the refractive indices of benzene, carbon tetrachloride, and water," J. Res. Natl. Bur. Stand. **67A**(2), 163–171 (1963).
23. J. Diaci, "Response functions of the laser beam deflection probe for detection of spherical acoustic waves," Rev. Sci. Instrum. **63**(11), 5306–5310 (1992).
24. S. J. Brockington, R. D. Horton, D. Q. Hwang, R. W. Evans, S. J. Howard, and Y. F. Thio, "Plasma density gradient measurement using laser deflection," Rev. Sci. Instrum. **76**(6), 063503 (2005).
25. L. W. Casperson, "Gaussian light beams in inhomogeneous media," Appl. Opt. **12**(10), 2434–2441 (1973).
26. G. Purves, G. Jundt, C. Adams, and I. Hughes, "Refractive index measurements by probe-beam deflection," EPJ Direct **29**, 433–436 (2004).

1. Introduction

High-power (kW) low-energy (mJ) electric pulses are implemented in a variety of industries and the near field physics for high strength (> 5kV/cm) electric fields applied in liquids has been of interest in a variety of industrial applications [1–6]. One such application, explores the interactions of electric fields with biology, observed on a cellular level *in-vitro* [1–6]. Specifically, high power short duration electric pulses have been shown to cause the phospholipid membranes of mammalian cells to become more permeable, while maintaining cell survivability via a process termed electroporation [3]. Electroporation of the cell membrane allows certain molecules to cross an otherwise impermeable membrane [3]. This technique is used for DNA transfection, drug delivery, and electrochemotherapy. A variety of eukaryotic cell types have been exposed to nanosecond electric pulses (nsEP) *in-vitro* and have exhibited electroporation via the uptake of propidium iodide (PI), trypan blue (TB), YO-PRO −1, and other membrane permeabilization indicators, into the cytoplasm. Over a decade of research has shown that short duration pulses (<1 μs) induce a variety of effects on cells, including induced apoptosis, cell organelle manipulation and stress responses [1–3]; however the correlation between driving mechanism and biological response is not well defined [1–3].

Nanosecond electric pulses (nsEP), are a subcategory of high power electric pulses ranging in duration from approximately 1 ns to 1 μs. The nsEP delivery parameters and mechanisms have been highly variable across the research spectrum, involving numerous

Optics EXPRESS

pulse characteristics, electrode geometries, poration indicators and physiological solutions. To complicate the correlation between biological response and driving mechanism, Ibey et al. [4,6,7] showed that pulse polarity and sequence modulates biological response. Bipolar pulses (i.e. positive voltage pulse followed by a negative voltage pulse) with the equivalent total duration of a single monopolar pulse, were less effective at inducing membrane permeabilization although the energy of the two pulse types were equivalent [7]. Bipolar and monopolar nsEP applied in conductive liquid (physiological solution) to cells *in-vitro* generate numerous multi-physics phenomena. These include thermal gradients, oxidation and reduction reactions at the electrode-liquid interface, electrophoretic motion of particles, and electrostriction/thermoelastic gradients which result in the generation of acoustic transients [8–17]. Biological effects induced *in-vitro* by high strength electric fields, can be a result of any of these phenomena and quantification of each phenomena is crucial to linking an observed biological response to its corresponding driving mechanism. Due to the nonuniformity of nsEP experimental parameters in past research, quantification of pulse dosimetry is required to correlate a driving mechanism to biological response.

This work focuses on the design and application of a passive optical imaging system utilized for quantification of thermal gradients and pressure fields generated through electrostriction and thermoelastic dynamics resulting from nsEP exposure. Specifically, the probe beam deflection technique (PBDT), is a passive optical sensing technique that has been utilized, in the past, to quantify acoustic transients and thermal gradients in 1-D with nanosecond temporal resolution [18]. In this paper a 2-D PBDT imaging system was designed and implemented to be relatively EMI immune and produce 2-D images of acoustic transients and thermal gradients near the electrode liquid interface during nsEP delivery. Specifically, the case of bipolar vs. monopolar nsEP was examined to quantify and image the thermal and pressure gradients produced by each respective pulse type.

2. Background

2.1 Probe beam deflection technique (PBDT)

The PBDT correlates the deflection of a laser beam propagating through a media of interest with any detectable thermal or acoustic disturbance in the media. This technique has been utilized extensively in the past, for ultrasound and photoacoustic measurement, as well as imaging [17–21]. The technique has been applied to the measurement of acoustic waves in gas phase, namely the gas coupled laser acoustic detector (GCLAD), where detection bandwidth is limited by the speed of sound in air [20,21]. PBDT has been shown to be a passive wide band ultrasonic sensor in liquids by multiple research groups [18–21]. Imaging of the ultrasonic target, such as soft tissue, has been demonstrated extensively in photoacoustics, and imaging of a photoacoustic wave has been shown [21]. Utilization of PBDT to measure acoustic waves generated by nsEP in 1-D has been shown by Roth et. al [18], however 2-D imaging of nsEP acoustic phenomena has not been demonstrated.

2.2 Short duration high power electric fields in biological media

The application of strong electric fields in polar and non-polar liquids has been studied extensively [8–10]. In the simplest cases, non-conductive solutions such as distilled water have been evaluated under fast rise time (ns) strong electric fields, applied via a variety of electrode geometries and have been shown to generate electrostrictive pressure gradients which result in acoustic transients [8–10]. When a polar liquid such as water, is exposed to an electric field, the molecules align with a dipole moment of $6.1\times10^{-30} C\cdot m$. In addition to dipole alignment, the dipoles also experience a strain on their bonds that is translated as a density gradient in the liquid [10]. The permittivity of a liquid is directly proportional to its density and temperature. Near the electrode where the field is the strongest, density rapidly decreases, causing amplification of the field and further amplification of the pressure gradient

Optics EXPRESS

[8]. If this pressure exceeds the tensile stress of the liquid and the hydrostatic pressure does not have time to compensate the electrostrictive pressure, cavitation forms near the electrode liquid interface, collapse of this cavity generates an acoustic wave [7–10].

The study of how short duration electric pulses affect biology has been of interest for the past decade [1–7]. Much of this work has been performed *in-vitro* in physiological solutions such as: phosphate buffered saline (PBS), and outside solution which have conductivities of approximately 1.3 S/m and are biologically compatible [1–7]. Electric field pulses applied to electrodes submersed in conductive solutions, produce high charge concentrations at the electrode liquid interface resulting from the reduction of load impedance as ion concentration increases. This condition yields electrochemical oxidation and reduction reactions in addition to the dissolution of water molecules yielding gas bubble formation at the anode [12]. Thermal gradients are generated in conductive media due to the electrophoretic motion of ions in the solution resulting in joule heating [12]. Acoustic generation in conductive media has been shown to be generated by both thermoelastic and electrostrictive mechanisms [9,10,17]. Thermoeleastic mechanisms such as photoacoustic generation, require that thermal confinement and stress confinement conditions must be met to generate an acoustic transient [17]. The pulse durations (600 ns, 1.2 μs) utilized in this work satisfy thermal confinement, however very little of the joule heating occurs within the stress relaxation time of the liquid and therefore thermoelastic acoustic generation plays only a supplemental role in combination with electrostriction to generate a pressure gradient in the physiological solution.

3. Theory

3.1 Probe beam deflection technique (PBDT)

Changes in refractive index are proportional to changes in density, the relationship can be seen in Eq. (1).

$$\delta n(\mathbf{r},t)=\left(\frac{dn}{d\rho}\right)_{\rho_0}\delta\rho(\mathbf{r},t) \tag{1}$$

This equation is derived from the Lorentz-Lorenz equation and has a practically accepted value of $3\times10^{-4}\ m^3/kg$ for distilled water [22]. Assuming a spherical wave front, the PBDT can be evaluated as a line integral along the beam path, integrating the refractive index gradient along the beams trajectory [23]. Much work has been done in theoretical formulating Gaussian beam deflection through heterogeneous mediums [23–26]. Utilizing a quadrant photodiode detector (QPD) or a knife edge detector, deflection magnitude as well as deflection angle [19], can be detected and correlated to the theoretical and bisectional photodiode (BPD) work done in the past [24]. Propagation of a Gaussian beam through heterogeneous media is governed by the paraxial ray equation shown in Eq. (2).

$$\frac{d}{ds}\left(n_0\frac{dr_v}{ds}\right)=\nabla_v n(\mathbf{r}) \tag{2}$$

n_0 is the refractive index of an undisturbed medium, r_v is the ray displacement in the normal plane of the ray, s is the arc length, and $\nabla_v n(\mathbf{r})$ is the projection of the refractive index gradient on the normal plane. The deflection angle is described by Eq. (3), and beam distance is described relative to the center of symmetry of the spherical acoustic wave.

$$\phi(l,t)=\frac{2l}{n_0}\int_l^{r_s}\frac{\partial n}{\partial r}\frac{dr}{\sqrt{r^2-l^2}} \tag{3}$$

Optics EXPRESS

Equation (2) can be converted into the form of Abel's integral and inversely, the refractive index along the trajectory can be derived from Eq. (3) and is shown in Eq. (4).

$$n(r,t) = -\frac{n_0}{\pi}\int_r^{r_s} \frac{\theta(l)}{\sqrt{r^2 - l^2}}\,dl \tag{4}$$

If the beam is stationary and the wave is propagating, the radial profile of the wave can be reconstructed from Eq. (4). These equations apply as long as the beam deflection is relatively small, i.e. the trajectory is not changed dramatically in regards to the refractive index magnitude along the trajectory.

A figure illustrating the spherical wave beam interaction geometry can be seen in Fig. 1.

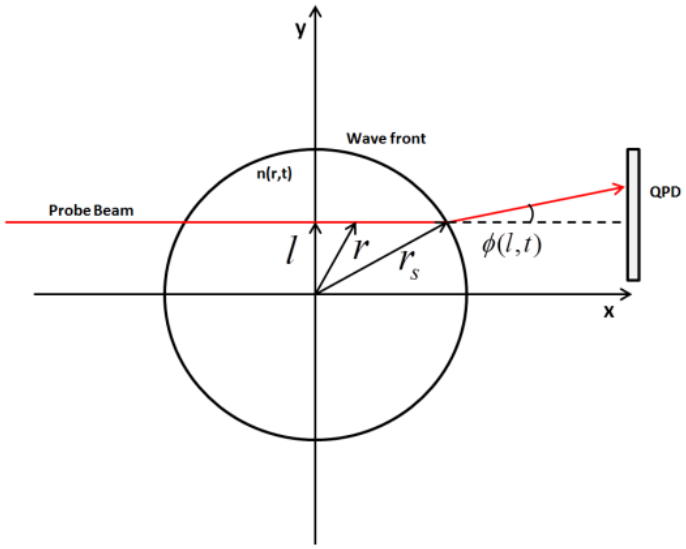

Fig. 1. Diagram of spherical wave probe beam interaction.

In Fig. 1, a quadrature photodiode (QPD) is pictured as the deflection measurement method. QPD's consist of four photodiodes configured in an array and provide the capability of measuring the propagation direction of the acoustic wave as has been shown in [11]. In this work the beam deflection sensing methodology is a knife edge-photodiode sensor, in which a deflection of the beam is measured as an optical intensity fluctuation at the photodiode. As has been discussed in [21], the sensitivity of the knife edge-photodiode sensor decreases with $\sin^2(\theta)$ where θ equals the angle formed by the intersection of the probe beam and the propagating acoustic wave. Bandwidth of the PBDT has been investigated by the GCLAD group [20] and is correlated to the beam waist and the attenuation of an acoustic wave in the propagation media. In this work, physiological media was chosen as the propagation medium and the 3 dB bandwidth of the PBDT as a product of probe beam waist is shown in Eq. (5).

$$f_w = \frac{c_l}{2\pi w} \tag{5}$$

Where c_l is the speed of sound in the physiological media (1500 m/s), and w is the probe beam waist (100 μm), thereby yielding a 3 dB bandwidth of approximately 2.4 MHz for the PBDT imaging system designed in this work.

Optics EXPRESS

3.2 Electrostriction in polar liquids

Electrostrictive pressure, is generated due to the relationship between permittivity and density as seen in Eq. (6).

$$\Delta P_{es} = \varepsilon_0 \rho \frac{\partial \varepsilon}{\partial \rho} \frac{E^2}{2} \tag{6}$$

In a polar liquid, the experimental results of Jacobs and Lawson [15] show the relationship between liquid density and permittivity, as can be seen in Eq. (7). The coefficient of the order of unity $k < 1.5$ in most polar liquids [10,15].

$$\rho \frac{\partial \varepsilon}{\partial \rho} \approx k \cdot \varepsilon \tag{7}$$

If an instantaneous voltage is applied to a spherical electrode submerged in a polar liquid, a bulk force is created with a density described by Eq. (8) [10].

$$f = -\nabla P_0 = -\nabla \left(P - \varepsilon_0 \rho \frac{\partial \varepsilon}{\partial p} \frac{E^2}{2} \right) \tag{8}$$

In polar liquids with free charge carriers, the dielectric loss factor ε'' must be considered when calculating the permittivity, the dielectric constant including the dielectric loss factor can be seen in Eq. (9).

$$\begin{aligned} \varepsilon &= \varepsilon' - j\varepsilon'', \\ \varepsilon'' &= \frac{\sigma}{2\pi f}. \end{aligned} \tag{9}$$

where σ is the conductivity of the medium and f is the bandwidth of the applied pulse.

In a liquid dielectric, the acoustic equation describes the flow and pressure of the liquid. In the case of electrostrictive acoustic generation, the bulk force resulting from the electric field applied to a spherical electrode submerged in water becomes the driving function in the acoustic equation as seen in Eq. (10) [9,10].

$$\begin{aligned} \frac{\partial W}{\partial t_1} + c\frac{\partial U}{\partial r_1} &= -\varepsilon_0 \frac{\partial \varepsilon}{\partial p} \frac{2E_0^{\,2} r_0^{\,4}}{c r_1^{\,5}}, \\ \frac{\partial U}{\partial t_1} + 2c\frac{W}{r_1} + c\frac{\partial W}{\partial r_1} &= 0. \end{aligned} \tag{10}$$

where $W = v/c$ is the ratio of liquid velocity to sound velocity, $U = \Delta\rho/\rho$ is the relative density change and E_0 is the electric field strength near the surface of the electrode tip (sphere). A full derivation of electrostriction in polar liquids can be found in [9–16].

4. Methods

4.1 COMSOL model of electromechanics in liquids

To model the state of stress in a liquid from and electromagnetic source, the electromagnetic stress tensor can be solved utilizing finite element methods [12]. The electromagnetic stress tensor can be seen in Eq. (11).

Optics EXPRESS

$$T_{EM,V} = -\left(\frac{1}{2}\varepsilon_0 \mathbf{E}\cdot\mathbf{E}\right) I + \varepsilon_0 \mathbf{E}\mathbf{E}^T$$
$$T_{EM,S} = \frac{1}{2}\left(\mathbf{E}\cdot\mathbf{D} + a_2 \mathbf{E}\cdot\mathbf{E}\right) I + \mathbf{E}\mathbf{D}^T + \frac{1}{2}(a_2 - a_1)\mathbf{E}\mathbf{E}^T \quad , \tag{11}$$

where, $T_{EM,V}$ is the electromagnetic stress tensor in the absence of a magnetic field, and $T_{EM,S}$ is the electromagnetic stress tensor in the absence of a magnetic field in an isotropic dielectric. a_1 and a_2 are the electrostrictive material properties, $\mathbf{D}$ is the electric displacement field, and $\mathbf{E}$ is the electric field. In a solid, a_1 corresponds to the change in permittivity resulting from elongation of the solid in a direction parallel to field, and a_2 corresponds to the change in permittivity resulting from elongation in direction perpendicular to the field. In an isotropic dielectric liquid the electrostrictive material properties can be represented by Eq. (7) as illustrated in Eq. (12).

$$a_1 = a_2 = \rho\frac{\partial \varepsilon}{\partial \rho} \approx k\cdot\varepsilon \tag{12}$$

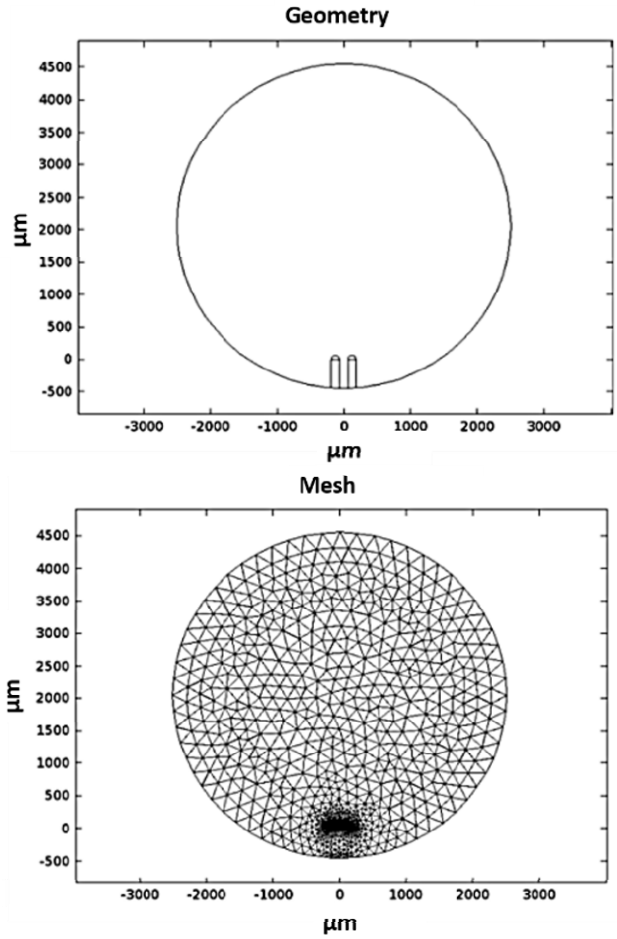

Fig. 2. (Top to Bottom) Geometry and mesh of 2-D FEM simulation of nsEP electromechanics.

Optics EXPRESS

A circular simulation domain was chosen, and electrodes were simulated as can be seen in Fig. 2. The domain was filled with saline solution with a conductivity of 1.3 S/m. The electrodes were modeled as rectangles with rounded tips. The width of the electrode gap was 150 µm, the electrode width was 125 µm, the length was 500 µm and the radius of the rounded electrode tip was 75 µm. To emphasize the near electrode physics, the node density of the mesh was chosen to be large near the electrode-liquid interface and smaller elsewhere in the domain. The boundaries of the domain were modeled as soft boundaries, absorbing all acoustic energy and producing no reflections. This boundary condition was chosen because initiation and propagation are the main focus of this work.

4.2 nsEP generator and dosimetry

The nsEP were applied by 127 µm diameter tungsten wire electrodes (A-M Systems, Sequim, WA) with a spacing of 160 µm. Each of the two wire electrodes was threaded through a 147 um polyimide tube (A-M Systems) such that all but 5 mm of the electrode was insulated. The two electrodes were stabilized by inserting the pair through a borosilicate capillary tube (World Precision Instruments, Sarasota, FL) and then fixed to a type-K connector (OMEGA Engineering Inc. Stamford, CT). All pulses were recorded on a Tektronix TDS-3054b Scope via a 100x probe.

The pulse width was set via a Stanford delay generator and a Pearson's coil was utilized to measure current in the circuit. The nsEP voltage and current pulses applied to electrodes submerged in outside solution (1.3 S/m), were measured at the electrodes and can be seen in Fig. 3.

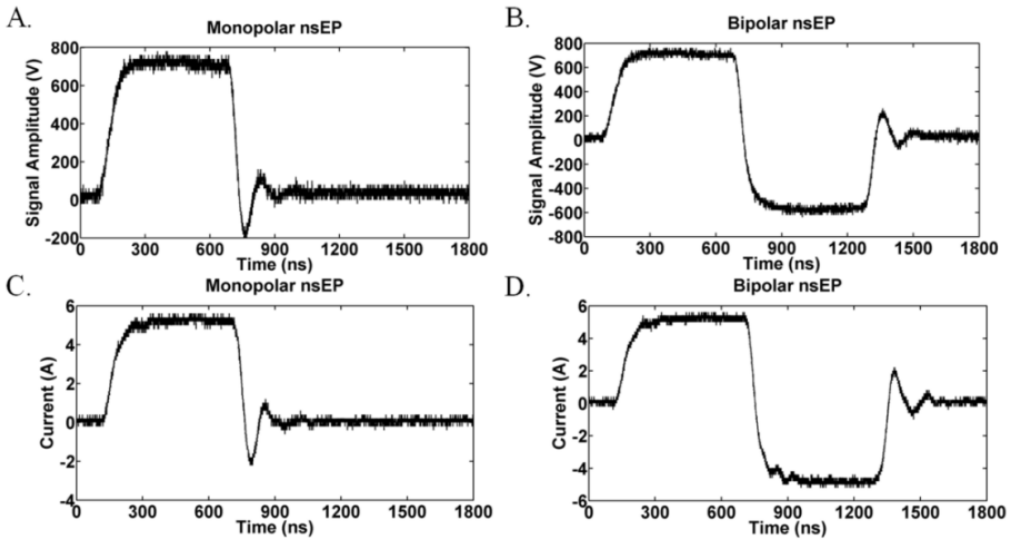

Fig. 3. A.) nsEP Voltage Waveform 600ns Monopolar, B.) nsEP Voltage Waveform 600ns Bipolar (1.2µs total duration), C.) nsEP Current Waveform 600ns Monopolar, D.) nsEP Current Waveform 600ns Bipolar (1.2µs total duration).

4.3 PBDT imaging system

A PBDT imaging system was designed to image thermal and acoustic phenomena resulting from nsEP applied via electrodes submerged in physiological solution. A platform was attached to three ThorLab stages, allowing for X, Y and Z stepped motion with a step resolution of 500 nm. A glass tank filled with a biologically-compatible buffer solution, consisting of (in mM) 135 NaCl, 5 KCl, 2 $MgCl_2$, 10 HEPES, 10 glucose, 2 $CaCl_2$, pH 7.4, 290-310 mOsm was placed on the platform. A 22 mW HeNe CW laser source was utilized as

Optics EXPRESS

a collimated beam, with a beam diameter of 100 µm and directed through the glass tank. After exiting the tank, the beam was focused with a 75 mm focal length convex lens onto a razor blade fixed to an XZ stage and positioned such that 50% of the focused beam was blocked. To ensure that approximately 50% of the beam was blocked, the razor blade was removed and the photodiode current I_{PD_Max} was recorded, then the laser was blocked and the photodiode current I_{PD_Min} was recorded. With the razor blade in the focal plane, the Z stage was adjusted, until the measured current was equal to $I_{PD\_Meas} = \frac{I_{PD\_Max} - I_{PD\_Min}}{2}$. A 75 mm focal length lens was placed 75 mm from the focal plane at the razor blade to recollimate the beam. The beam was then directed into a coupling lens attached to an SMA connector threaded to a 1 mm core 5m long fiber optic cable. The other end of the fiber was connected to a SI diode with a 1 ns rise time via an SMA connector. The electrodes utilized were fixed to the platform such that the electrodes/tank and laser beam could be moved independently. The PBDT system was optimized to measure displacement deflections as a result of the knife edge positioned at the focal point of the L1 lens. The PBDT signals recorded were mostly from double deflections (beam displacement) resulting from the beam deflecting during entry and exit of a radial acoustic wave front. Single deflections (angular deflections) resulting from interactions with thermal gradients were slightly attenuated due to the positioning of the lens however nsEP thermal gradients create much larger deflections relative to nsEP pressure transients, therefore, resulting in thermal PBDT signals with sufficient SNR for acquisition. A diagram of the system can be seen in Fig. 4.

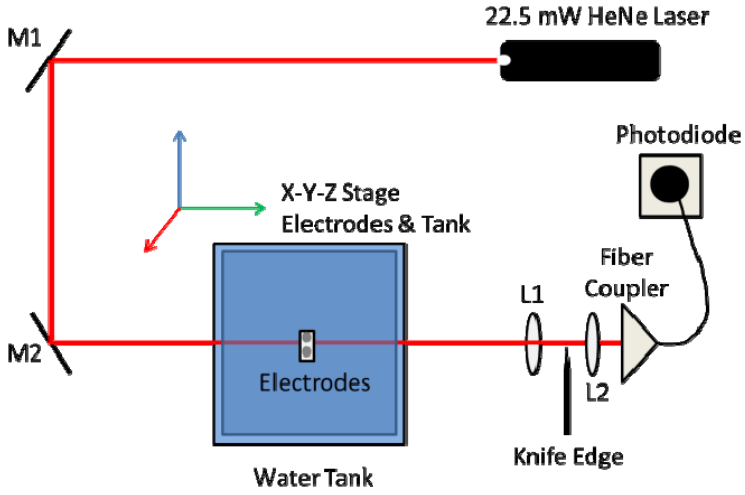

Fig. 4. PBDT Imaging system diagram.

Signals were acquired for each beam position of the scan and indexed according to beam position in a 3D matrix with X and Z corresponding to beam position and the Y axis corresponding to temporal samples. The scan range of the system was 170 mm along the x-axis and 14 mm along the z-axis. Some images were acquired with a shorter scan range along the x-axis. Each PBDT signal consisted of 50000 samples acquired at a sample rate of 2 GHz. Acquisition of the PBDT signals was initiated at the time the nsEP was delivered via a Tektroniks oscilloscope connected to a PC. All signals were relayed to a National Instruments LabVIEW program that was developed as an XYZ stage controller and data recorder. The tank was moved 0.5 mm, the nsEP generator was triggered at 5 Hz, 50 signals were recorded, averaged and saved in a text file, the tank was then moved 0.5 mm and the process was repeated. Data visualization was accomplished utilizing two methods:

Optics EXPRESS

1. Single line scans (B-Mode), with high spatial step resolution, were reconstructed as 2D images with width (y-axis) correlated to the number of beam positions, length (x-axis) correlated to the number of temporal samples, and the pixels intensity correlated to signal amplitude. Imaging of a photoacoustic wave was performed in a similar manner (B-mode) by the GCLAD group [20,21], as seen in Fig. 5.
2. Multiple line scans (M-Mode), with low spatial step resolution, were reconstructed as multi-frame time-lapse videos. The width (y-axis) of each frame was correlated to the number of beam positions in the z direction, length (x-axis) correlated to the number of beam positions in the x direction, and the number of frames correlated to the number of temporal samples. Each beam position was imaged as a pixel of a frame and each temporal sample set represented a complete frame as seen in Fig. 6.

The Tektroniks oscilloscope was connected to a PC. All signals were recorded in a National Instruments LabVIEW program that was developed as an XYZ stage controller and data recorder. The tank was moved 0.5 mm, the nsEP generator was triggered at 5 Hz, 50 signals were recorded, averaged and saved in a text file, the tank was then moved 0.5 mm again and the process was repeated. A total of 1000 point scans were obtained in approximately 2 hours.

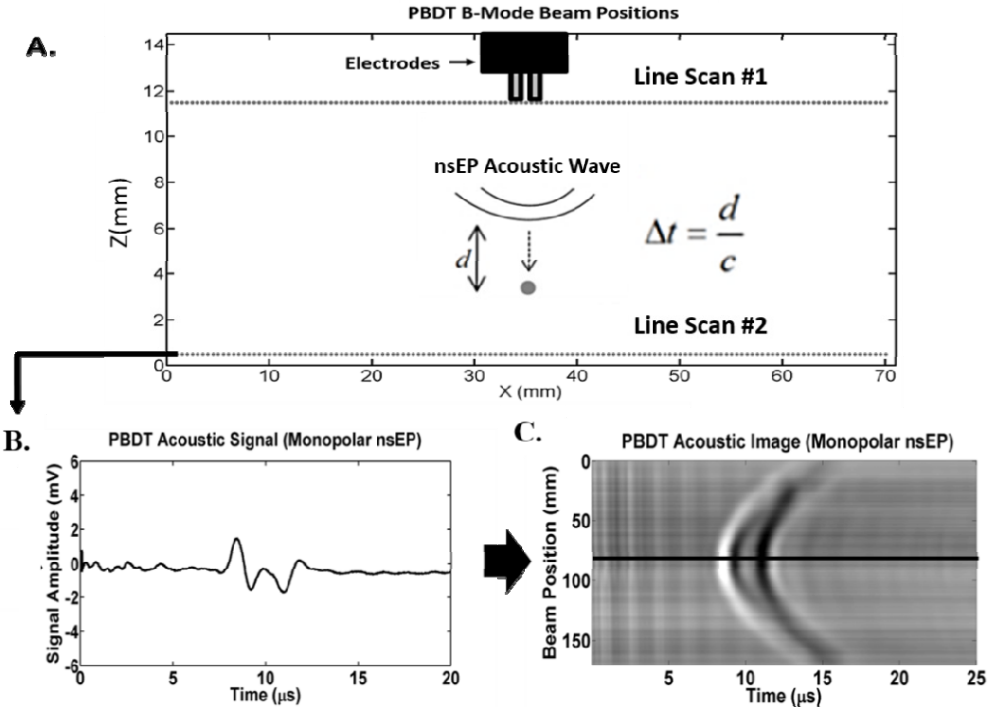

Fig. 5. B-Mode single line scan methodology. A.) Line Scan methodology. B.) 1-D PBDT signal acquired when acoustic wave propagates past beam at the velocity c, the speed of sound in liquid . C.) Example image illustrating how each 1-D PBDT signal represents a strip of the reconstructed 2-D PBDT image.

Optics EXPRESS

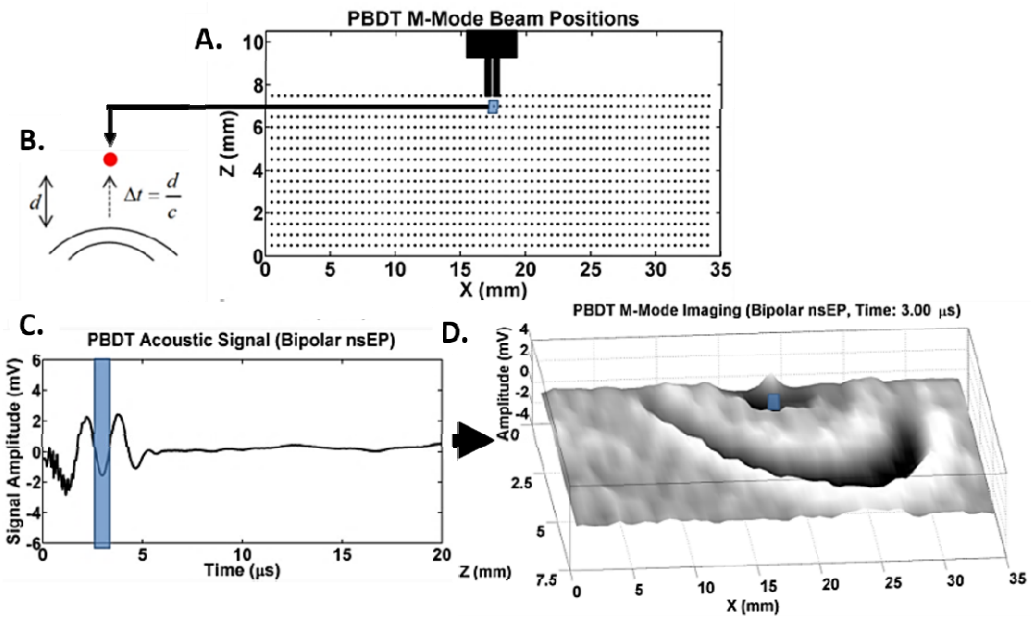

Fig. 6. M-Mode multiple line scan methodology. A.) M-Mode PBDT scan methodology. B.) Diagram of Acoustic wave propagating past optical beam. C.) 1-D PBDT signal acquired when acoustic wave propagates past beam, blue box is a segment of 1-D signal converted into a frame of the time-lapse image sequence. D.) Time lapse imaging frame where blue box represents a pixel (Beam Position) at the 3 μs frame (1-D signal temporal sample).

5. Results

5.1 COMSOL electromechanics model

Transient electromechanic solutions were acquired for a duration of 1.4 μs for monopolar and 1.2 μs for bipolar nsEP excitations. The domain pressure was recorded every 200 ns, and a gray-scale colormap was chosen to emphasize the transient wave shape. The time series simulation for the monopolar nsEP excitation can be seen in Fig. 7.

Optics EXPRESS

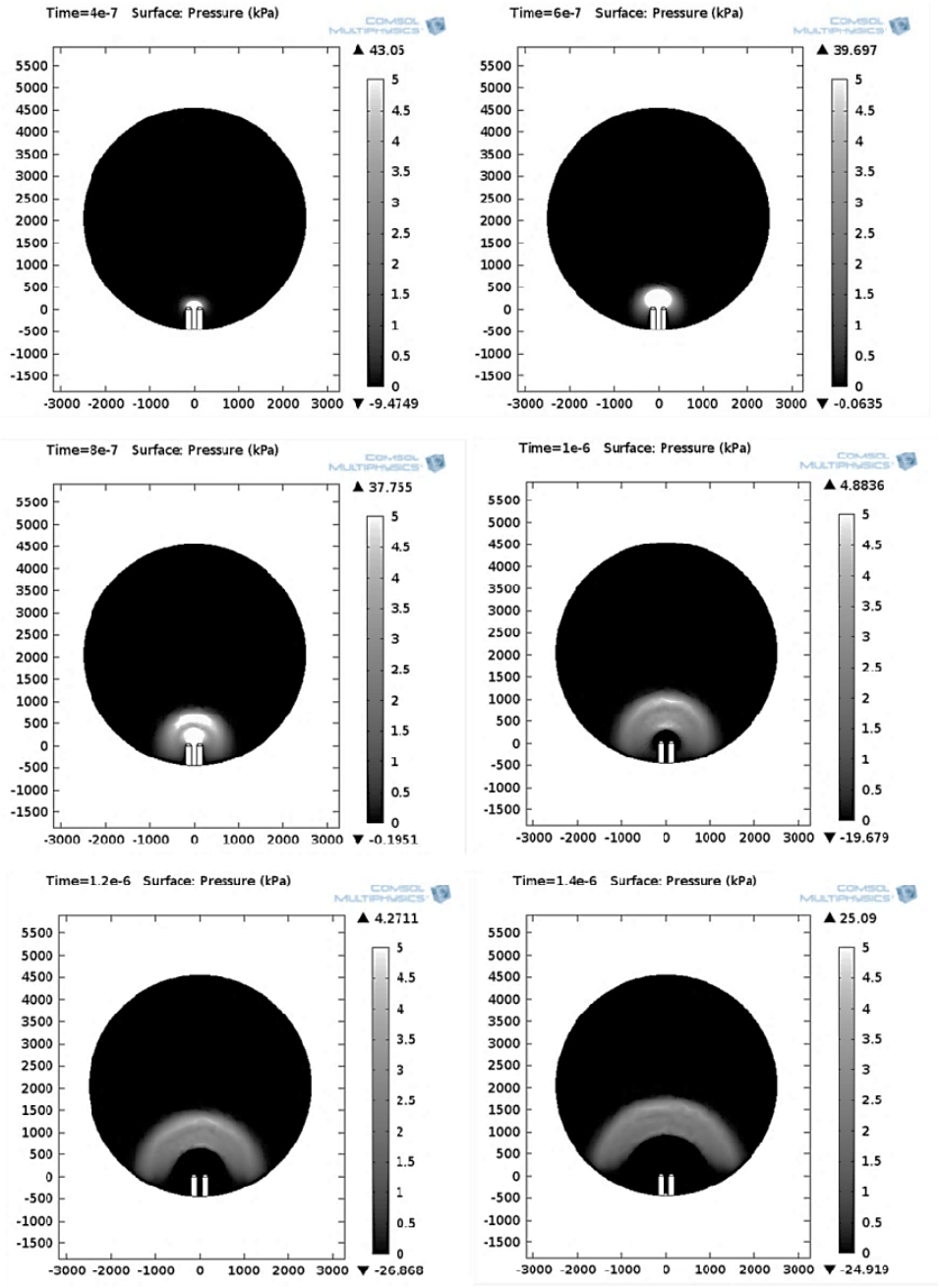

Fig. 7. COMSOL electromechanics simulation results of electrostrictive acoustic generation from a monopolar nsEP (Duration: 400 ns-1.4μs, Interval: 200 ns per frame).

The monopolar nsEP excitation produces a single wave front emitted from between the electrodes and propagating radially away from the electrodes. The electromechanic pressure field time series for the bipolar nsEP excitation can be seen in Fig. 8.

Optics EXPRESS

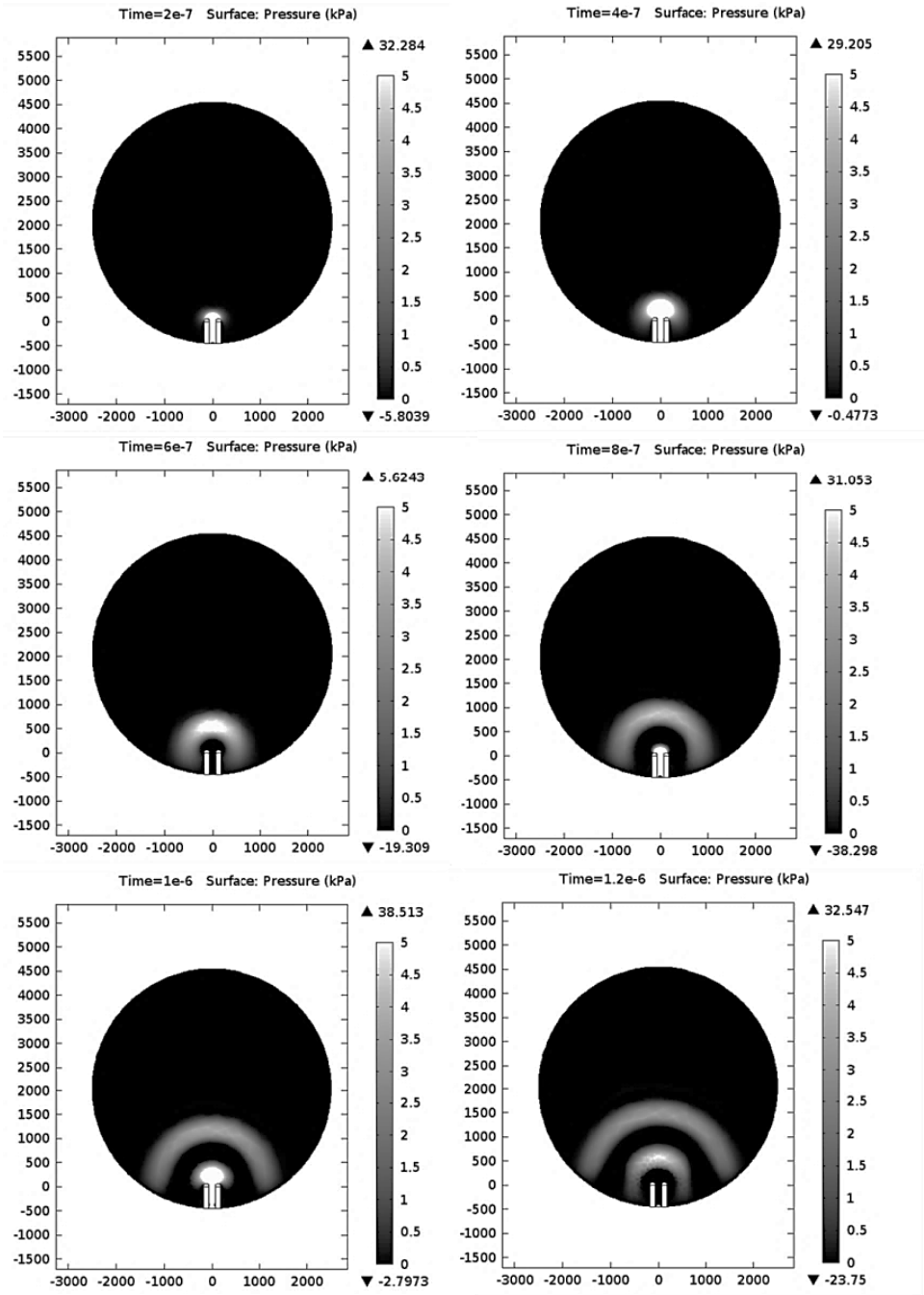

Fig. 8. COMSOL electromechanics simulation results of electrostrictive acoustic generation from a bipolar nsEP stimulus (Duration: 400 ns-1.2μs Interval: 200 ns per frame).

5.2 1-D probe beam deflection signals

Beam deflection was measured with a knife edge and a photodiode as illustrated in the diagram in Fig. 4. Incident optical intensity fluctuations resulting from deflection across the knife edge were recorded on an oscilloscope as mV dynamic range signals with a time

Optics EXPRESS

resolution of 500 ps. At each beam position, 50 nsEP were applied, PBDT signals were recorded for each pulse, and the recorded signals were averaged.

With the beam waist edge in contact with the electrodes tips, thermal signals were acquired. Bipolar (600 ns-600 ns) and monopolar (600 ns) nsEP were applied and PBDT signals were recorded. EMI generated from the nsEP appears as noise in each signal, at the time the nsEP was initiated. To measure physical phenomena near the electrode, EMI was suppressed such that the acoustic and thermal signals can arrive at the same temporal instance as the EMI and still be resolved as a result of a sufficient SNR. To qualitatively compare the total thermal energy deposited, as a result of monopolar and bipolar nsEP, PBDT thermal signals were acquired for a duration of 22 μs following a pulse event and can be seen in Fig. 9.

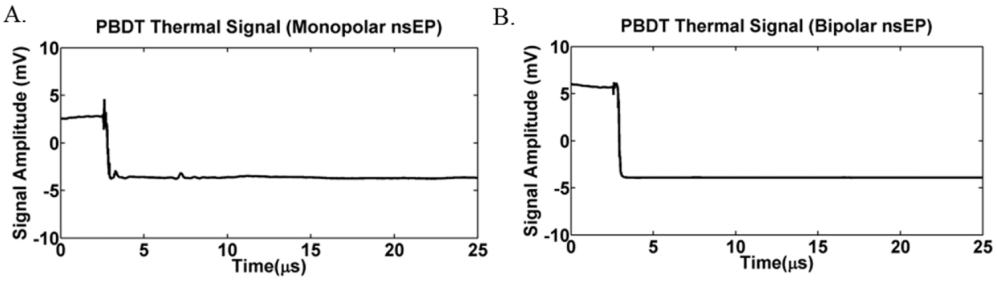

Fig. 9. PBDT thermal signals acquired with electrodes partial intersecting beam waist A.) Monopolar nsEP B.) Bipolar nsEP.

To confirm the thermal nature of these PBDT signals, a longer duration (35ms) acquisition was performed to illustrate the thermal relaxation after a monopolar nsEP exposure. This acquisition is shown in Fig. 10.

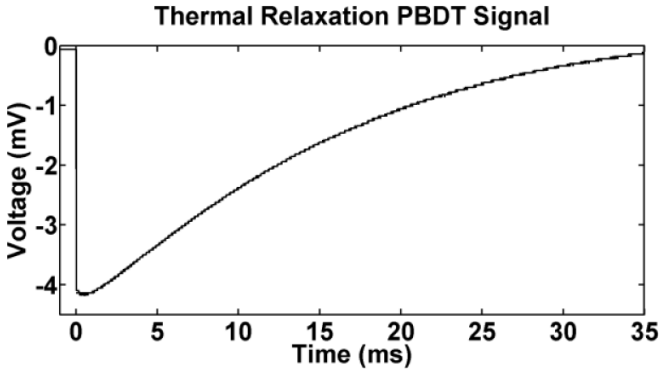

Fig. 10. PBDT monopolar thermal signals acquired with electrodes partial intersecting beam waist (35 ms acquisition to capture thermal relaxation).

Acquisition of the acoustic disturbances was accomplished by moving the beam such that the electrodes were no longer partially blocking the beam. The beam was positioned 100 μm below the electrodes and acoustic signals were recorded. 1-D acoustic signals are shown in Fig. 11.

Optics EXPRESS

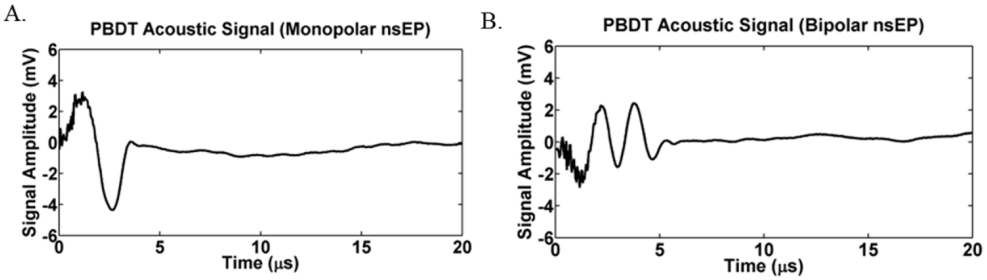

Fig. 11. PBDT Acoustic signal acquired 100 μm from electrodes A.) Monopolar nsEP B.) Bipolar nsEP.

The probe beam was then moved 4mm directly below the electrode tips. At this beam position the acoustic signals were temporally displaced from the nsEP EMI, as a result of the delayed time of acoustic arrival. The 1-D acoustic signals acquired 4 mm below the electrodes can be seen in Fig. 12.

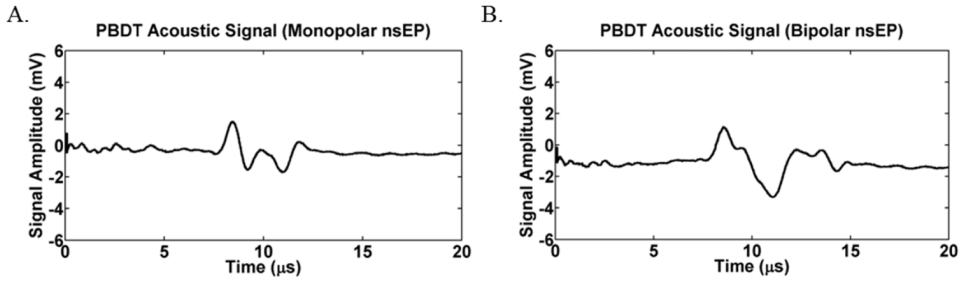

Fig. 12. PBDT Acoustic signal acquired 12 mm below electrodes A.) Monopolar nsEP B.) Bipolar nsEP.

The velocity of the transient pressure wave was measured by recording time of arrival and distance traveled. Equidistance beam positions, with 5 mm spaces, were chosen and the time of arrival for a selected wave was recorded at each beam position. The temporal trajectory of the transient wave can be seen in Fig. 13.

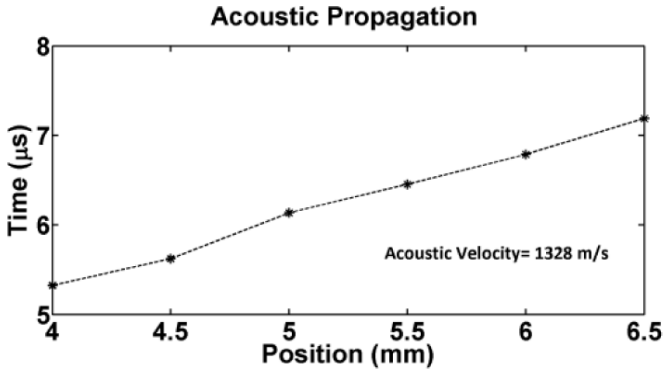

Fig. 13. PBDT Acoustic propagation velocity.

The velocity of the pressure transient was calculated to be approximately 1328 m/s; in close agreement with the speed of sound in water of 1500 m/s.

Optics EXPRESS

5.3 Single frame (B-mode) acoustic and thermal imaging

The 1-D signals were stacked based on line scan position, normalized and mapped to a gray scale color map. The images were visualized in 2-D with gray value representing PBDT signal magnitude and 3-D with surface plot height representing PBDT signal magnitude. The images recorded in the near field contain low amplitude EMI appearing as high frequency noise in the images represented by shade variations (2-D Image) and height variations (3-D Surface Plot) near the pulse initiation time (0 µs). The images acquired 100 µm from the electrode interface can be seen in Fig. 14.

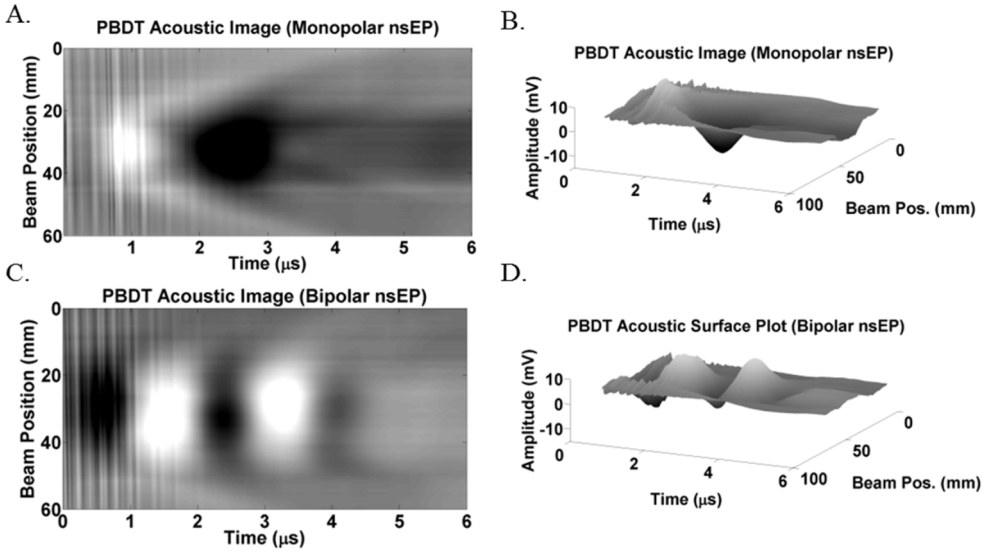

Fig. 14. PBDT images and surface plots acquired 100 um below electrodes A.) 600 ns monopolar nsEP acoustic image, B.) 600 ns monopolar nsEP acoustic image surface plot, C.) 1.2 µs bipolar nsEP image (600 ns per pulse), D.) 1.2 µs bipolar nsEP surface plot (600 ns per pulse).

Far field images were acquired at a distance of 4mm from the electrode tips. The images are shown with time represented by the x-axis and the horizontal beam position represented by the y axis. The acoustic waves traverse the beam resulting in a temporal beam deflection profile. The images can be seen in Fig. 15.

The images shown in Fig. 15 are in very close agreement to images acquired in the past utilizing strobe photography or schlieren imaging by other groups, however, these systems are EMI susceptible and require systems with timing jitter less than 100 ns for this application [8,9]. The unique method of beam deflection acquisition per pixel, via beam stepping, enables time resolution exceeding pulsed schlieren photography. The acoustic nature of the measurements is discussed and verified in further detail in [18] and the speed of the wave was verified in Fig. 13. The images acquired from the monopolar nsEP exposures show a single period wave with a clearly defined high and low pressure region. The bipolar nsEP exposure images show a multi period wave that seems to mimic the positive and negative voltage swing of the input pulse.

Optics EXPRESS

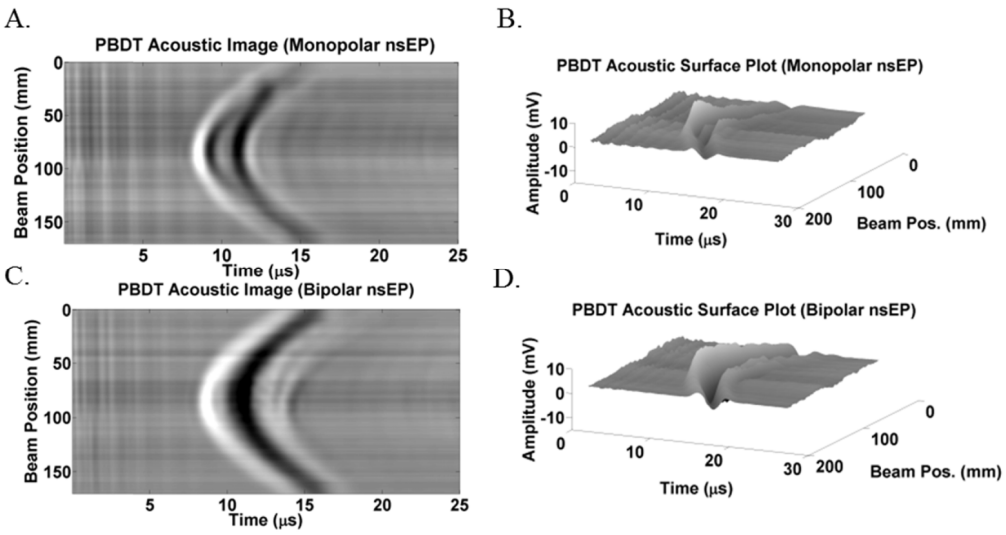

Fig. 15. PBDT images and surface plots acquired 12 mm below electrodes A.) 600 ns monopolar nsEP image, B.) 600 ns monopolar nsEP surface plot, C.) 1.2 μs bipolar nsEP image, D.) 1.2 μs bipolar nsEP surface plot.

5.4 Multi frame (M-mode) acoustic and thermal imaging

Both monopolar and bipolar nsEP exposures were imaged utilizing the M-mode technique. The photodiode utilized to acquire deflection signals, had a sample frequency of 2 GHz or 0.5 ns time resolution. Each time step acquired was converted to a 13 pixel (length) by 68 pixel (width) frame, however, for the sake of brevity only 1 μs steps are shown. The electrodes were centered at coordinates (x,z) at location (17,0). The nsEP was initiated at time step 0μs. The time-lapse images acquired from the monopolar nsEP exposure can be seen in Fig. 16 and Fig. 17.

Optics EXPRESS

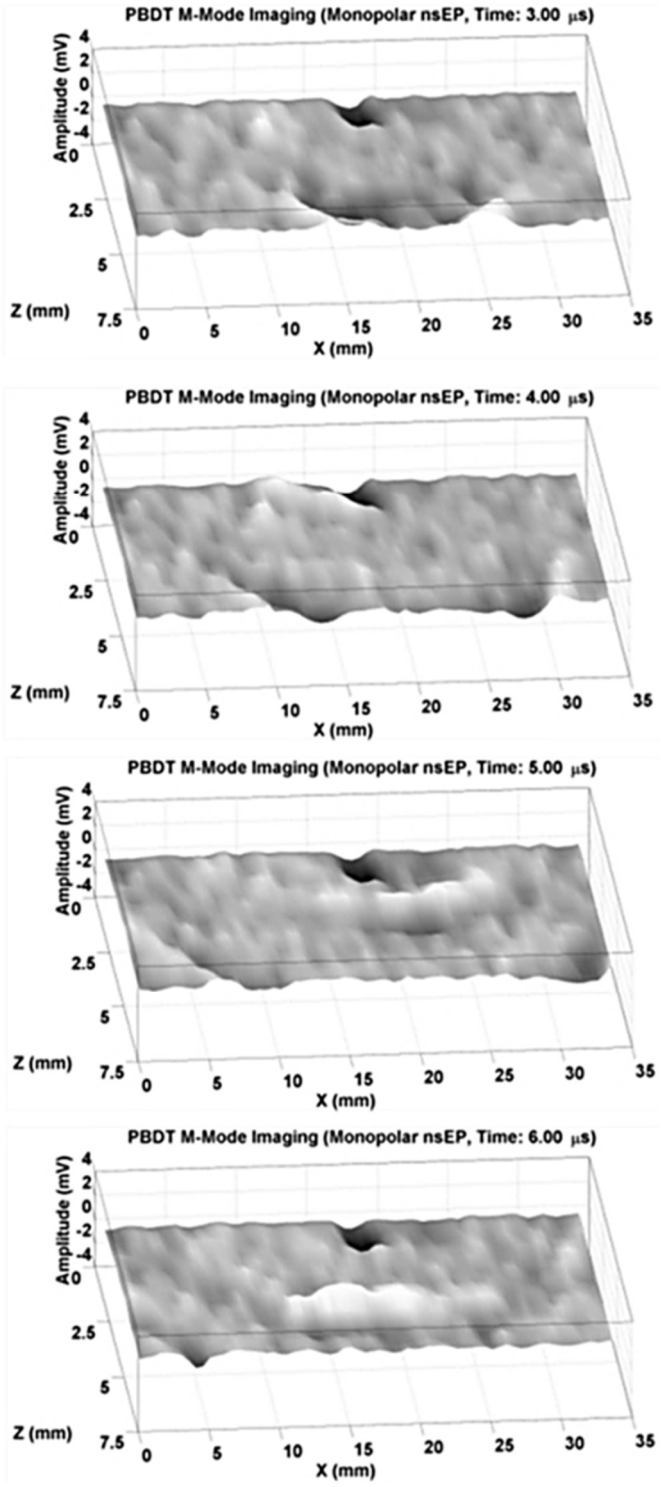

Fig. 16. PBDT time-lapse thermal and acoustic imaging of a monopolar nsEP (Duration: 0 μs-2 μs Interval: 1 μs per frame.

Optics EXPRESS

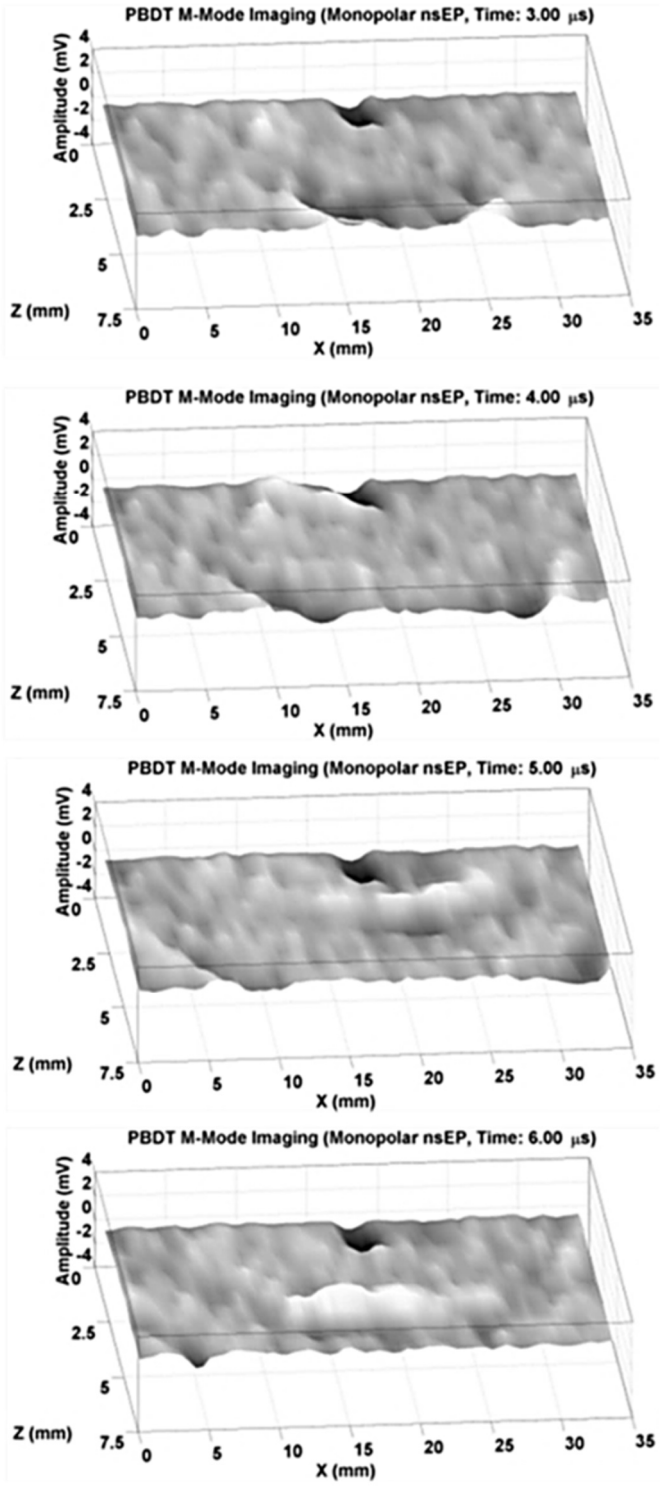

Fig. 17. PBDT time-lapse thermal and acoustic imaging of a monopolar nsEP (Duration: 3 μs-6 μs Interval: 1 μs per frame.

Optics EXPRESS

The bipolar nsEP exposure can be seen in Fig. 18, and Fig. 19. In this time-lapse series the bipolar pulse generates a less turbulent bipolar acoustic disturbance that propagates away from the electrodes at a velocity of 1328 m/s.

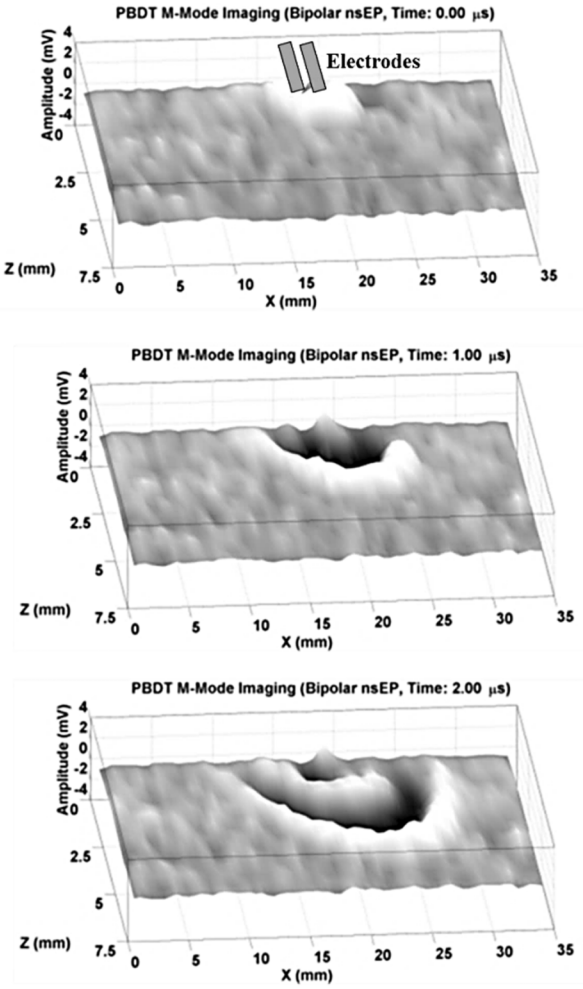

Fig. 18. PBDT time-lapse thermal and acoustic imaging of bipolar nsEP (Duration: 0 μs-2 μs Interval: 1 μs per frame.

Optics EXPRESS

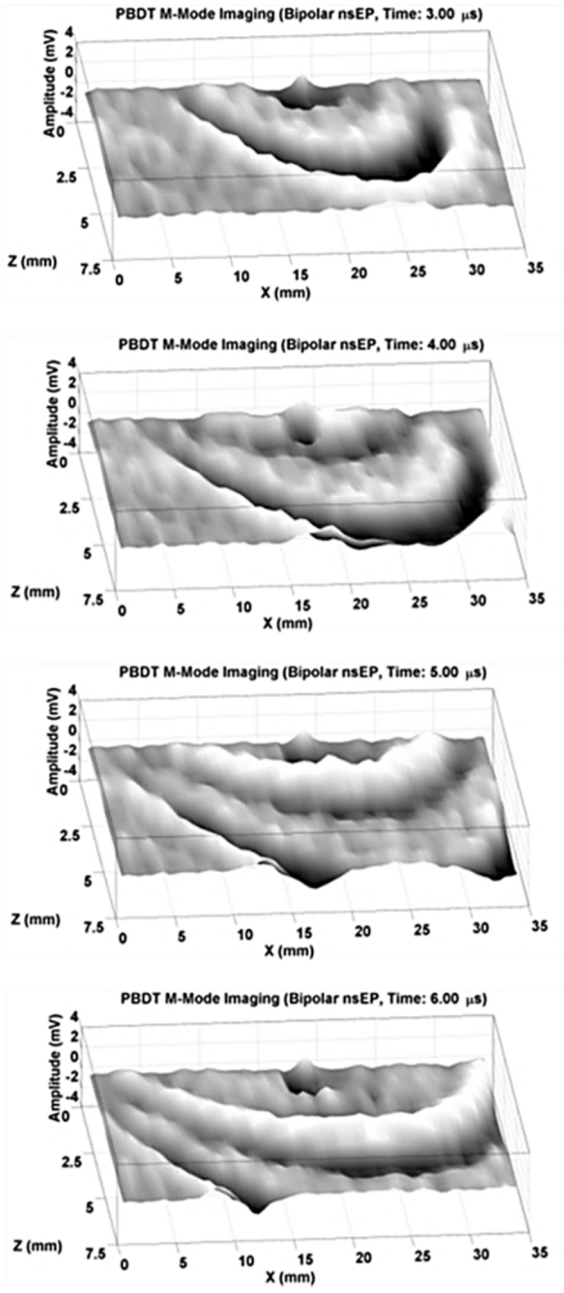

Fig. 19. PBDT time-lapse thermal and acoustic imaging of bipolar nsEP (Duration: 3 μs-6 μs Interval: 1 μs per frame.

Thermal excitation can be seen in Fig. 16, Fig. 17, Fig. 18 and Fig. 19 as a surface depression at (x,y) coordinate (17,0) in each frame of the surface plot. This corresponds to the position of the electrodes in the time-lapse series. The thermal depression is generated at the time the pulse is initiated, grows during the pulse duration, and requires multiple milliseconds to relax back to steady state after the pulse is terminated. Due to the short duration of the acquisition (9 μs) the thermal relaxation is not shown in these images, however, as shown

Optics EXPRESS

previously in Fig. 10, the 1-D signal showing the relaxation confirms the thermal nature of this image characteristic.

6. Discussion

6.1 PBDT dosimetry capabilities

The PBDT provides the capability to passively image acoustic and thermal phenomena in liquids exposed to high strength electric fields where traditional piezoelectric transducers cannot be implemented. The ability to measure and image both thermal and acoustic phenomena passively enables dosimetry quantification for other directed energy applications other than nsEP including but not limited to, radio frequency dosimetry, infrared pulse neural stimulation, and laser treatment dosimetry. M-mode PBDT rendering further improves dosimetry quantification by providing time-lapse visualizations that can be correlated directly to measured biological responses acquired with imaging techniques such as streak camera imaging and fluorescence based confocal microscopy.

6.2 PBDT imaging vs. Schlieren limaging

Traditional schlieren imaging is similar to probe beam deflection in that a beam is being deflected and partially blocked along after the focal plane such that any deflection is seen by the detector as a shift in incident optical energy. However, schlieren strobe photography requires the use of a camera and short pulse (< 20ns) laser with low timing jitter (< 50ns) to acquire time series images of fast dynamics. The PBDT, however, replaces the camera with a single photodiode with fast response time (< 2ns) and the short pulse laser with a CW laser source. The assumption made in this work is that the measured physical phenomena are stable and consistent for each nsEP exposure making it possible to acquire signals over many nsEP exposures and combine them into a single image or time-lapse series. In such cases where this assumption is not true, time-lapse photography with comparable time resolution to PBDT imaging would require high repetition rate (> 2 GHz), short pulse duration (< 1ns) lasers. PBDT exhibits greater image contrast then schlieren imaging in that the laser beam can be focused into a diffraction limited small interaction area thereby amplifying the deflection of the beam and increasing signal to noise ratio (SNR) at the detector. If the multi-shot stability assumption is met, PBDT increases time resolution and image contrast with decreased implementation costs. In addition, passive EMI immune sensing due to the reduction in electrical interfaces such as cameras and EMI susceptible laser triggers is possible. Passive sensing provides the inherent advantage of real time acquisition of dosimetry data during high strength electric field cell exposure and can be utilized to correlate biological response to driving mechanism in the future.

6.3 Monopolar vs. bipolar nsEP multi-physics dosimetry

The PBDT images acquired improve dosimetry for nsEP exposures by improving scientific intuition into nsEP exposure physics through visualization. Specifically in the case of bipolar vs. monopolar nsEP cellular response, the distinction between the shape of the monopolar acoustic waves and the bipolar waves illustrates a distinct difference in post pulse conditions. This pressure discrepancy is much more prevalent in the images acquired 100 μm below the electrodes then those acquired further away as seen in Fig. 14 and Fig. 15. As the acoustic waves propagate away from the electrodes, the multi peaked bipolar wave takes the shape of a single period wave front. This discrepancy would be difficult to identify if the phenomena could not be observed near the electrode. The passive EMI suppressed performance of the PBDT imaging system allows for this observation.

The source of this acoustic emission resulting from an nsEP was investigated experimentally and through modeling in this work. The wave front characteristics for each pulse type have been reproduced by an electromechanics model. The significant difference in

Optics EXPRESS

acoustic wave shape between monopolar and bipolar nsEP exposures and the close agreement with the electromechanical modeling results, leads us to believe that the electrostrictive mechanism is the dominant mechanism of acoustic generation in nsEP exposures. The correlation between the acoustic waveform and calculated electric field temporal signal leads us to believe that thermoelastic mechanisms do not dominate. One of the main issues in understanding the mechanisms of electroporation is the characterization of the insults the cell actually experiences during nsEP exposure. Much of the work done in the nsEP field focuses on the driving electric field as the sole cause of the electroporation phenomena, through charging of the membrane, and the subsequent response of the cell due to this induced charge [1–4]. The phospholipid membrane of a cell, however, is a dielectric separating the cytoplasm (intracellular) of the cell from the outside solution (extracellular). Therefore the phospholipid membrane can be charged via an applied electric field or a change in membrane thickness. Pressure fields generated as a result of the applied electric field may be able to generate the membrane charge required to induce electroporation, thereby leading us to believe that the electric field component may not be solely responsible for poration of the cell, an effect that is seen in techniques such as sonoporation where the high strength electric field does not exist.

In addition to the polarization of the cell membrane due to the pressure component of nsEP exposure, the pressure gradients generated by nsEP also affect the electric field distribution in the solution. Both electrostriction and thermoeleastic effects lead to anisotropic permittivity gradients resulting from the relationship between permittivity, temperature, and pressure generating anisotropic electric field distributions. When biological targets, such as eukaryotic cells, are exposed to nsEP their positioning between the pulse delivering electrodes may play a role in the observed biological response.

Quantification of both thermal and pressure gradients was demonstrated with PBDT and PBDT imaging improves visualization of multi-physics dosimetry. Though there seems to be significant differences in the electrostrictive and thermoelastic behavior of bipolar and monopolar pulses, conclusions related to electroporation are still difficult to make, however mapping and visualizing pressure and thermal excitation with cellular scale PBDT resolution (<10 μm) for *in-vitro* nsEP experiments in the future, may help correlate driving mechanism to biological response.

7. Conclusions

In conclusion, the PBDT was used to acquire both 1-D, 2-D and time-lapse images of multi-physics dosimetry phenomena resulting from nsEP exposure through passive optical imaging driven mitigation of EMI. Though these images were acquired on a spatial scale far larger than the cellular scale, this technique can be adapted for imaging on a cellular scale by approaching the defraction limit of a PBDT beam and the application of a focused beam to replace the collimated beam utilized in this work. The lack of variability in physical phenomena produced by each nsEP in a pulse train i.e. event stability, combined with a repetition rate slow enough to eliminate thermal additivity, enables high speed and contrast imaging. Though the spatial resolution of these images was quite large, in comparison to the size of a eukaryotic cell, the feasibility of this technique for directed energy dosimetry, has been demonstrated in this work.

Acknowledgment

Portions of this research were performed while the author held an NRC Research Associateship award at the Air Force Research Laboratory, JBSA Ft. Sam Houston, Texas.